CHEMISTRY OF MATERIALS

pubs.acs.org/cm

Article

Interplay between Intrinsic Thermal Stability and Expansion Properties of Functionalized UiO-67 Metal–Organic Frameworks

Isabella Goodenough, Venkata Swaroopa Datta Devulapalli, Wenqian Xu,* Mikaela C. Boyanich, Tian-Yi Luo, Mattheus De Souza, Mélissandre Richard, Nathaniel L. Rosi, and Eric Borguet*

Cite This: *Chem. Mater.* 2021, 33, 910–920

Read Online

ACCESS | Metrics & More | Article Recommendations | Supporting Information

ABSTRACT: The UiO family of metal–organic frameworks (MOFs) has been extensively studied for several applications owing to their high stability rendered by their robust secondary building units. The efficient design and use of these materials require a fundamental understanding of their thermal stability and its impact on chemical and structural functionality. Herein, we provide a detailed characterization of the intrinsic thermal behavior of the UiO-67 and functional analogues, UiO-67-NH_2 and UiO-67-CH_3. Using *in situ* temperature-programmed X-ray diffraction, we find that distortion of the carboxylate group on the organic linker leads to negative thermal expansion (NTE) of the UiO-67 MOFs during heating. This NTE behavior is correlated with rich and reversible thermal changes observed in the MOF infrared spectral signature as samples are heated to the sample activation temperature (473 K). We find that in the absence of oxygen, activated UiO-67 samples show higher thermal stability compared to ambient or inert environments, with temperature-programmed desorption revealing an overall stability trend: UiO-67 > UiO-67-CH_3 > UiO-67-NH_2. Two stages of change are observed during thermal treatment above 473 K, which are directly related to deformation of the inorganic node and the isotropic NTE behavior of these materials. Ultimately, these results provide a real-time interpretation of the fundamental thermoresponsive behavior of UiO-67 MOFs and offer a foundation for accurate interpretation of MOF interactions with guest molecules and their temperature dependence.

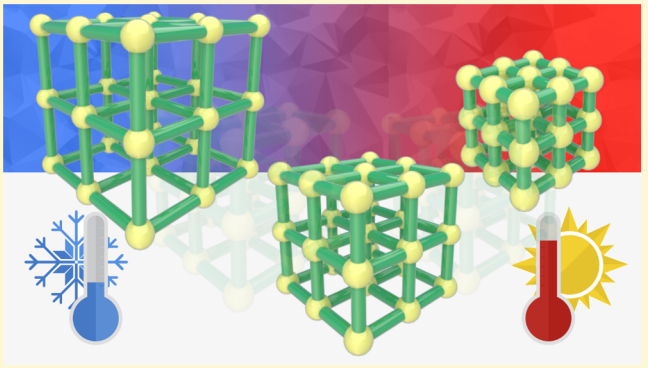

INTRODUCTION

Metal–organic frameworks (MOFs) constitute a broad class of porous, crystalline materials which have shown promise in a wide variety of applications, including gas storage and separation,[1,2] sensing,[3,4] and catalysis.[5] These materials are hybrid inorganic–organic structures that can be synthesized from a multitude of metals or metal oxides and organic building blocks, resulting in a virtually infinite number of possible structures.[6−8] Unlike other porous materials, like porous carbons or zeolites, MOFs' amenability toward modular design allows for direct control over chemical and physical properties and thus offers a high degree of tunability to achieve desired attributes.[6,7,9,10] However, MOF functional properties are heavily influenced by their thermal stability.[8,11,12] In this regard, thermal stability is defined as the ability of the material to resist variations in structural, chemical, and functional properties in response to temperature changes.[13] Despite many practical applications requiring some *a priori* knowledge of MOF thermal stability, there is a lack of experimental insight into the intrinsic thermal properties of these materials other than the thermal decomposition processes, which warrants the need for a thorough evaluation of the influence of temperature on MOF structural and functional properties.

In this work, we focus on zirconium-based MOFs as this class of materials is often acclaimed for their exceptional chemical,[14−16] mechanical,[17−19] and thermal[14,20] stabilities compared to other subgroups of MOFs.[5,7,8] Isostructural UiO-66 and UiO-67 (UiO = University of Oslo) are representative examples. In an ideal crystal of UiO MOFs, the inorganic node consists of a Zr_6 octahedron supported by coordination of μ_3-bridging hydroxyl and oxo groups and 12 bridging carboxylates from ditopic carboxylate linkers giving rise to a 3D periodic framework.[21,22] Previous studies on UiO MOFs recognized that the $Zr_6O_4(OH)_4$ node is sensitive to thermal treatment in which the cluster can reversibly dehydrate by changing the coordination number of the Zr metal centers.[14,15,23] This

Received: October 2, 2020
Revised: December 4, 2020
Published: December 30, 2020

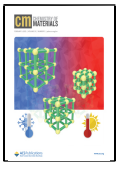

https://dx.doi.org/10.1021/acs.chemmater.0c03889
Chem. Mater. 2021, 33, 910–920

process has been observed experimentally *via in situ* infrared (IR) spectroscopy and gravimetric analysis over the temperature range of 523−573 K under inert and ambient environments, whereby the fully hydrated $Zr_6O_4(OH)_4$ node loses two equivalents of water and transitions to its fully dehydrated (Zr_6O_6) form.[15,23] This structural change is not reported to compromise the structural integrity of the MOF. However, extended X-ray absorption fine structure analysis revealed significant structural distortions of the cluster resulting from the change in Zr coordination number.[15] Moreover, *in situ* analysis of the X-ray pair distribution function revealed that the Zr_6 nodes of UiO-66 and NU-1000 compress with increasing temperature, and that these distortions are linked to perturbations in the MOF local structure without affecting the long-range crystal structure.[24] These structural distortions are related to phase changes in the bulk metal-oxide (ZrO_2) and may be associated with reversible changes of the zirconium node during dehydration.[15,24]

Several reports relate MOF thermo-structural properties with thermal expansion behavior. In particular, negative thermal expansion (NTE)—the decrease in volume with increasing temperature—has been observed in a handful of MOFs, including MOF-5,[25] HKUST-1,[26] IRMOF variants,[27] ZIFs,[28] and UiO materials.[27,29] This unusual phenomenon is believed to originate from several low-frequency transverse vibrational modes of the organic linker and inorganic cluster, which enables a degree of structural flexibility.[12] Recently, Burtch *et al.* implemented several design strategies to control thermal expansion properties in MOFs by investigating the effect of ligand sterics, metal identity, guest environment, and thermal history on MOF NTE.[27] Their proof-of-concept study has provided detailed insight into designing MOF materials with controlled thermal expansion behavior.

Ultimately, only limited experimental studies exist which directly probe the influence of temperature on the structural evolution of UiO MOFs without decomposing the material. Furthermore, these studies have focused primarily on the inorganic component (metal node) leaving a lack of understanding about the role of the organic component on thermal stability. While it is generally accepted that the decomposition pathway for UiO materials proceeds *via* the breakdown of the ligand, producing benzene and CO_2 as the gaseous decomposition products and leaving the bulk metal-oxide (ZrO_2), it remains unclear whether the evolution of these volatile species forms primary or secondary decomposition products.[11,15,30] The decomposition temperature for UiO-66 and UiO-67 have been reported *via* thermogravimetric analysis (TGA) within the range of 673−773 K under ambient and inert environments.[11,30−32] However, the reported temperatures depend heavily on the measurement conditions and this justifies for the need for a more detailed description of the thermal processes which occur during MOF degradation.

Understanding the dynamics resulting from heating-induced effects is critical for comprehending structural changes and framework stability. Without a complete knowledge of the intrinsic thermal behavior, the interactions between porous materials and guest species can be easily misinterpreted.[33,34] In this work, we investigate the fundamental thermal behavior of UiO-67 MOFs using temperature-programmed Fourier-transform infrared spectroscopy (FTIR), mass spectrometry (MS), and synchrotron powder X-ray diffraction (PXRD) under controlled vacuum conditions which isolate the material of interest by eliminating atmospheric contaminants such as water vapor, carbon dioxide, or nitrogen gas and thus provide ideal conditions for monitoring thermally induced framework changes. PXRD measurements reveal significant NTE behavior of the UiO-67 MOFs, which we find to be associated with reversible structural changes observed in the IR signature. Our work provides insights into intrinsic framework behavior that governs fully reversible heating effects of UiO-67, UiO-67-NH_2, and UiO-67-CH_3 as samples are heated up to 473 K *via in situ* FTIR and synchrotron PXRD. With the goal of elucidating changes and/or processes that take place as MOFs are heated above 473 K, temperature-programmed desorption mass spectrometry (TPD-MS), *in situ* FTIR, and PXRD are used to track the evolution of structural changes during the degradation process.

EXPERIMENTAL SECTION

The syntheses of UiO-67, UiO-67-NH_2, and UiO-67-CH_3 are based on the established method reported in detail previously.[35] From our previous work, we estimated the defect concentration for all three UiO-67 MOFs using elemental microanalysis and found that for activated UiO-67 samples, the average concentration of missing linker defects per secondary building unit (SBU) is less than one for UiO-67, equal to one for UiO-67-NH_2, and 1.6 for UiO-67-CH_3.[35] These results are in good agreement with the ligand occupancy characterized by XRD refinement (0.97 for UiO-67 and 0.93 for UiO-67-NH_2) (see Section 2.2 in the Supporting Information for more details).

Temperature-programmed IR and MS experiments were performed using custom-built ultrahigh vacuum (UHV) instruments described previously.[36] Briefly, a stainless steel UHV chamber was pumped down using a turbomolecular pump backed by a mechanical pump providing base pressures of less than 1.0×10^{-8} Torr after bakeout. Samples were deposited onto a clean 25 μm thick tungsten (W) grid (AlfaAesar) braced to a copper sample manipulator. Sample temperature was monitored by a fast response K-type thermocouple (Omega) directly spot-welded to the W grid. This design allows for rapid cooling to cryogenic temperatures (~100 K) and resistive heating up to 1400 K using direct current from a power supply (model # SCR 10-80, Electronic Measurements Inc.).

For TPD-MS and FTIR experiments, MOF samples that were dispersed in dimethylformamide (DMF) were first centrifuged at 14,000 rpm for 5 min after which the supernatant was removed. The remaining wet MOF pellet (~2 mg) was pasted onto the W grid as a disk of 6−8 mm diameter and thickness of about 25−50 μm to provide uniform coverage with an optical density on the order of 1, as evaluated by FTIR, and introduced into the UHV chamber. The chamber was baked over a period of 18−24 h, during which the temperature of the sample and chamber reached a maximum of 373 K. Sample activation was achieved post-bakeout by holding the MOF samples at 473 K for 1 h.

Custom-written LabVIEW programs, using drivers from commercial components, were used to control the heating process, monitor temperature and pressure, and track the evolution of mass fragments. Mass spectra were acquired during heating of the MOFs from 300 to 1273 K at 2 K/s continuously. Decomposition products were verified using a shielded residual gas analyzer (RGA) quadrupole mass spectrometer (AccuQuad RGA 300, Stanford Research Systems). Thermally induced changes were monitored in real time by collecting *in situ* IR spectra using an FTIR spectrometer (Tensor 27, Bruker) *via* OPUS 7.5 software (Bruker). Spectra were acquired in the transmission mode in the range of 400−4000 cm^{-1} as an average of 16 scans using a room temperature DLaTGS detector with 4 cm^{-1} resolution (6 mm aperture and 10 kHz scan velocity). The total time for the completion of a spectrum was ~14 s. Before each experiment, a 64-scan background spectrum was collected using the bare tungsten grid as the sample reference.

Temperature-programmed synchrotron PXRD experiments were performed at Beamline 17-BM at the Advanced Photon Source at the Argonne National Laboratory (ANL). The beamline uses a VAREX

https://dx.doi.org/10.1021/acs.chemmater.0c03889
Chem. Mater. 2021, 33, 910−920

4343CT area detector to harvest *in situ* 2D XRD data in the X-ray transmission geometry. Sample powder was loaded into a one-end sealed amorphous silica capillary (O.D. 1.1 mm, I.D. 0.9 mm), which was mounted to a sample stage connected to a turbomolecular pump that maintained a vacuum status of lower than 1.0×10^{-6} Torr during the experiments. Two temperature programs were used on each of the three MOFs: (1) cycling of temperature between 90 and 480 K and (2) thermal degradation from room temperature to 900 K. In the temperature cycling experiment, a sample was first activated at 473 K (373 K for UiO-67-CH_3) to remove physically absorbed species in the framework before cooling to 90 K, while XRD data were continuously collected every minute. Then, the sample was heated from 90 to 480 K followed by cooling back to 90 K in a step mode with a 30 K interval, where XRD data were taken at each interval. In the thermal degradation experiment, a sample was heated from room temperature to 900 K at a rate of 60 K/min, while XRD collection was continuous with a rate of 10 s per XRD image. Temperature control was achieved either by an Oxford Cryostream 800 Plus instrument in the temperature cycling experiment or by a hot air blower used in the degradation experiment. The X-ray wavelength was 0.35364 Å. Data conversion from 2D to 1D was carried out through the GSAS-II software.[37] TOPAS (version 5) was used for Rietveld analysis.

RESULTS AND DISCUSSION

Initial Characterization. The initial IR spectra of the UiO-67 MOFs under UHV conditions reveal several narrow and intense features consistent with previous reports for crystalline nanoporous materials.[15,30,38,39] The IR spectra of UiO-67 upon introduction into the UHV chamber ($P < 5.0 \times 10^{-6}$ Torr) and following sample activation at 473 K ($P < 1.0 \times 10^{-8}$ Torr) are presented in Figure 1. It is evident for UiO-67 that

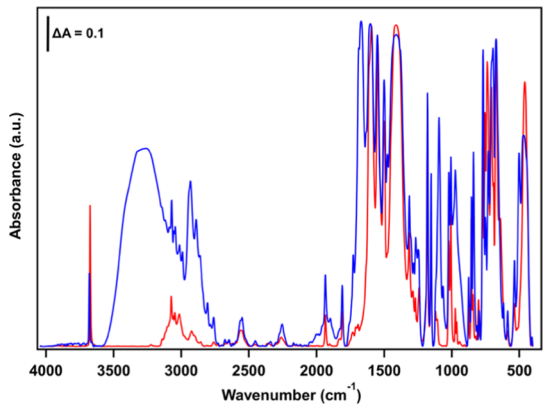

Figure 1. IR spectra of UiO-67 recorded upon introduction to the UHV chamber ($P < 5.0 \times 10^{-6}$ Torr) (blue) and following sample activation at 473 K ($P < 1.0 \times 10^{-8}$ Torr) (red). All baseline corrected spectra were recorded at room temperature.

prior to sample activation, a broad band centered at 3440 cm^{-1} dominates the high wavenumber region of the IR spectrum, which is assigned to residual physisorbed water and hydrogen bonded solvent (DMF). Moreover, intense features at 2930, 2856, and 1668 cm^{-1} are consistent with the C−H and C−N stretching of pore-confined DMF, which vanish with activation at 473 K.[15,23] Similar IR spectral features are observed for UiO-67-NH_2 and UiO-67-CH_3 (Figures S1 and S2). Assignment of vibrational modes is guided by previous literature reports and can be found in the Supporting Information (Table S1) for all UiO-67 MOFs.[15,23,30,39]

The choice of sample activation temperature was guided by our prior work, which used IR and TGA to evaluate the activation protocol for UiO-67 and functional analogues, UiO-67-NH_2 and UiO-67-CH_3.[35] TGA of the as-synthesized samples revealed negligible weight loss between 423 and 673 K, indicating that the samples may be stable up to 673 K, while evaluation of the IR spectral signature revealed no significant spectral changes after activation at 473 K to suggest degradation of the framework (Figures 1, S1, and S2).[35]

All MOFs studied in this work feature a single, narrow isolated O−H stretch at 3678 cm^{-1} attributed to a symmetric and equivalent distribution of bridging μ_3-OH groups around the zirconium node (Figures 1, S1 and S2).[23,40] This feature increases in intensity with the removal of physisorbed water and solvent. Functionalization of the biphenyl dicarboxylate (BPDC) linker is confirmed for UiO-67-NH_2 by the presence of bands at 3485 and 3398 cm^{-1} representative of asymmetric and symmetric N−H stretching modes, respectively (Figure S1).[41] For UiO-67-CH_3, features at 2982 and 2962 cm^{-1} are associated with asymmetric and symmetric sp^3 C−H stretching modes, respectively, of the methyl substituent (Figure S2).[42] Functionalization does not appear to influence the nature of the isolated O−H stretch (3678 cm^{-1}) as the band position and width are consistent for all UiO-67 MOFs.

Sample purity is confirmed by synchrotron PXRD under high vacuum conditions ($P < 1.0 \times 10^{-6}$ Torr) during the activation process (Figure S11). The activation at 473 K (373 K for UiO-67-CH_3) removed almost all adsorbed solvent molecules in the frameworks revealed by the notable intensity change of several low 2θ angle peaks, for example, 3.3 and 4.8° (Figure S11). However, a gradual increase of structural disorder (static atomic displacement) in the sample crystallites was observed through the disappearance of high 2θ angle XRD features when samples were held at the activation temperature for an extended period of time, evidenced by an overall reduction in high angle peak intensity. For this reason, and in order to retrieve the greatest amount of structural information from the XRD data, the samples were cooled from the activation temperature to 300 K as soon as no further changes in the low 2θ angle XRD peaks were observed (~10 min).

Reversible Thermal Effects. A number of unique and reversible changes appear in the IR spectra upon heating from 100 K to 473 K. The free bridging hydroxyl mode—$\nu(OH)_{free}$—initially observed at 3678 cm^{-1} (100 K) for all UiO-67 MOFs broadens and shifts toward lower wavenumber with increasing temperature; at 473 K, this feature is observed at 3670 cm^{-1} (Figure 2). Furthermore, by 473 K, the intensity of $\nu(OH)_{free}$ increases on the order of 50% for UiO-67, while the intensity for the functionalized analogues remains virtually unchanged (Figure 2). After thermal treatment and upon cooling to 100 K, the $\nu(OH)_{free}$ signal returns to its initial state and overlaps almost perfectly with the initial spectra measured prior to heating, indicating fully reversible thermal behavior. Multiple heating cycles have been carried out for different sample batches to confirm reproducibility (see Figure S3).

An increase in the $\nu(OH)_{free}$ intensity observed for UiO-67 has been previously reported to result from solvent removal and subsequent emergence of cornerstone μ_3-OH groups that were initially perturbed by solvent-induced hydrogen bonding.[23] However, analysis of the IR spectra following activation (Figure 1) provides no spectroscopic evidence to suggest that residual DMF or water remains in the interior pore space. Should this intensity increase in $\nu(OH)_{free}$ result from the desorption of perturbing solvent molecules during heating, then we should expect to observe the loss of a hydrogen-bonded IR signal associated with the solvent. Given that no

https://dx.doi.org/10.1021/acs.chemmater.0c03889
Chem. Mater. 2021, 33, 910−920

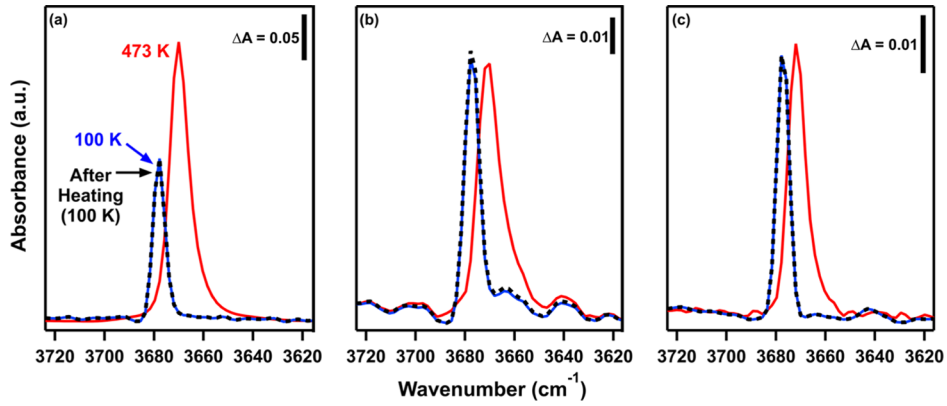

Figure 2. IR spectra highlighting the thermally induced changes of $\nu(OH)_{free}$ for (a) UiO-67, (b) UiO-67-NH_2, and (c) UiO-67-CH_3, as shown before heating at 100 K (blue), during heating at 473 K (red), and after heating at 100 K (black, dashed). Note blue and black traces for UiO-67, UiO-67-NH_2 and UiO-67-CH_3 lie directly on top of one another.

such signal is observed suggests that the observed redshift and increase in $\nu(OH)_{free}$ intensity for UiO-67 are purely thermal effects.

To completely understand the impact of temperature on the MOF structure, temperature cycling experiments were carried out under high vacuum ($P < 1.0 \times 10^{-6}$ Torr) and monitored using *in situ* XRD. The evolution of the UiO-67 unit cell edge length as the temperature is cycled from 90−480−90 K (Figure 3) clearly reveals a negative linear relationship between

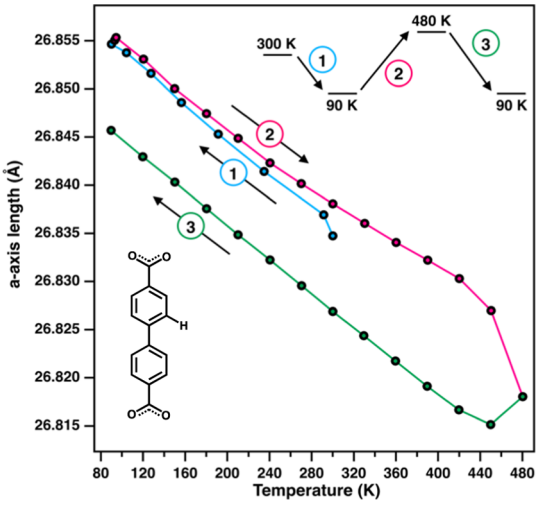

Figure 3. Change in the unit cell edge length (Å) for UiO-67 as sample temperature is cycled from (1) 300 to 90 K (blue), (2) 90 to 480 K (magenta), and (3) 480 to 90 K (green), as represented by the schematic experimental sequence in the inset. The associated error in *a*-axis length is smaller than the symbol size.

the axis length and temperature. All three UiO-67 MOFs exhibit isotropic NTE (Figure S13). For UiO-67, a sharp decrease is observed around 480 K (Figure 3), which correlates to an irreversible increase of the Zr atomic displacement parameter (ADP), signaling an increase of static disorder of the Zr site (Figure S15). The origin of this irreversible change is related to the Zr node dehydroxylation discussed in the next section. Other than this, the linear NTE behavior is mainly attributed to the change of bond lengths and angles in the carboxylate group, according to the Rietveld refinement results (Figures S16 and S17). The C−O bond length and O−C−O bond angle change from 1.259(5) Å and 129(1)° at 90 K to 1.227(6) Å and 134(1)° at 480 K, resulting in a compression of the O−C−O triangle by 0.07 Å. It is important to note that the bond lengths and angles measured by XRD are based on average atomic site positions obtained from Rietveld refinement. The C−O bond length reported above is in fact the distance between the average positions of the C and O sites, the apparent decrease of which upon heating is likely a result of correlated vibrational motion between C and O, while the actual C−O bond length is unlikely to decrease. Moreover, the refinement results also reveal that the dihedral angle of the phenyl rings in the BPDC ligand varies reversibly with temperature (Figure S18).

Functionalization on the organic linker impacts the degree of NTE in the UiO-67 MOFs. Examination of the linear thermal expansion coefficients (α) during temperature cycling from 90−480−90 K for the three MOFs (Table 1) reveals that UiO-67-NH_2 and UiO-67-CH_3 have smaller NTE coefficients than UiO-67. This may be because the functionalized branches on the BPDC linkers render the crystal lattice less compressible during heating to 480 K, an effect also discussed in the study by Burtch *et al.*,[27] However, both functional analogues show larger lattice contraction than UiO-67 at ~480 K (Figure S13), which is correlated to the loss of μ_3-OH groups from the node and described in detail in the next section. A comparison of the XRD data measured at 300 K for the three activated MOFs reveals that both UiO-67-NH_2 and UiO-67-CH_3 have a higher degree of structural disorder than UiO-67, as shown by the relatively weak high 2θ angle peaks of UiO-67-NH_2 and UiO-67-CH_3 compared to UiO-67 (Figures S19−S21). Besides, UiO-67-NH_2 and UiO-67-CH_3 are more susceptible to increasing structural disorder than UiO-67 upon heating, as

Table 1. Linear Thermal Expansion Coefficients (α) of UiO-67 Series MOFs [10^{-6} m/(m·K)] Calculated from Refined Unit Cell Parameters[a]

	temperature cycling		thermal degradation	
	calculated range (K)	α	calculated range (K)	α
UiO-67	90 to 420	−3.29(1)	570 to 790	−8.7(1)
UiO-67-NH_2	120 to 330	−2.48(7)	580 to 740	−9.5(3)
UiO-67-CH_3	120 to 300	−1.06(7)	580 to 770	−3.13(6)

[a]See Figures S13 and S25 for details.

https://dx.doi.org/10.1021/acs.chemmater.0c03889
Chem. Mater. 2021, 33, 910−920

shown by the weakening or disappearance of high 2θ angle peaks after a cycle of heating and cooling (Figures S19–S21) because of defect generation in the crystal structures as the sample temperature approaches 480 K. In any case, the higher degree of structural disorder of the functional analogues does not impact the structural integrity of the bulk material.

Analysis of the IR difference spectra in the 1750–1050 cm^{-1} interval provides insights into thermally induced structural changes associated with carboxylate (C–O) and benzene ring stretching, C–H bending, and N–H bending (UiO-67-NH_2).[15,43] Several IR features in this region are shifted toward lower wavenumber (redshift) and grow in intensity with increasing temperature, as shown in Figure 4 for UiO-67.

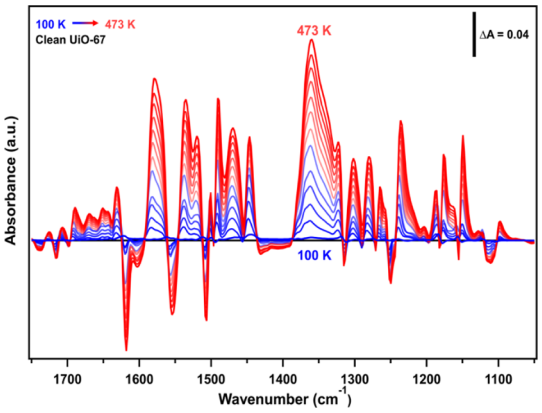

Figure 4. IR difference spectra for UiO-67 in the 1750–1050 cm^{-1} region recorded *in situ* during heating from 100 K (blue) to 473 K (red), as indicated by the color legend showing changes in carboxylate, benzene ring, and C–H bending modes. Difference spectra were collected using the clean MOF at 100 K as the reference (black).

Similar profiles for the functionalized analogues are provided in the Supporting Information (Figures S4 and S5). These thermally induced spectral changes are most likely related to the changes in the biphenyl dihedral angle and lattice contraction evidenced by XRD (Figures S15–S18). However, it is important to report that these thermally induced perturbations do not irreversibly change the MOF structure evidenced by the observation that upon sample cooling to 100 K, all spectral features return to their initial state and that no new vibrational features appear, indicating that all UiO-67 MOFs are stable with respect to heating in UHV up to 473 K.

For UiO-67, the most notable vibrational signals are observed at ∼1360 and ∼1580 cm^{-1} and assigned to the symmetric and asymmetric C–O stretching modes of the bidentate Zr-coordinated carboxylate group, respectively (Figure 4).[44] Recall, that the largest contributor to the linear NTE behavior of the three MOFs are the changes in the C–O bond length and O–C–O bond angle of the carboxylate groups (Figures S16 and S17). Changes in the IR difference spectra, specifically of the C–O stretching modes, indicate significant structural distortions on the carboxylate groups during heating. Taken together, it follows that thermal perturbations of the carboxylate moieties on the organic linker are likely the main contributor to the NTE behavior for the three MOFs.

The vibrational motions of UiO-67-NH_2 are uniquely affected by temperature changes. Specifically, the sharp ν(N–H) bands detected at 3485 and 3398 cm^{-1} (100 K) show substantial spectral broadening toward higher wavenumber (blueshift) and an apparent reduction in intensity when heated to 473 K (Figures 5 and S6). This thermal response occurs

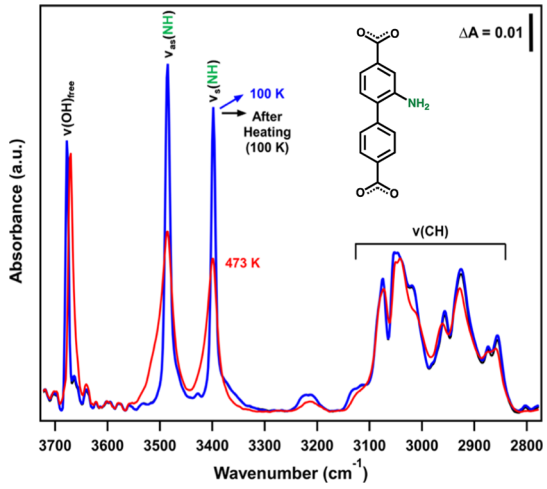

Figure 5. IR spectra of UiO-67-NH_2 recorded before heating at 100 K (blue), at 473 K (red), and after heating at 100 K (black), highlighting temperature-induced changes in MOF features associated with the bridging free O–H on the Zr node (3678 cm^{-1}), primary N–H stretching (3486 and 3398 cm^{-1}), and linker C–H modes. Note: blue and black spectra lie almost directly on-top of one another, indicating that this heating effect is reversible. All spectra are baseline corrected.

gradually and is not influenced by the heating rate within the 1.0–2.0 K/s range. It is important to report that the ν(N–H) peak area is conserved after heating and that the signal recovers to its initial state upon cooling back to 100 K, indicating that no NH_2 groups are removed during the heating process. The gradual broadening and reduction in the IR peak height of the N–H stretching modes (Figures 5 and S6) correlate with large atomic displacement of the linker atoms and wider dihedral angle between the planes of the benzene rings, which causes greater variation of local environments for the NH_2 groups that contributes to the broadening of the IR peaks (Figures S18 and S28). A similar thermal response is observed for the methyl C–H stretches (2982 and 2962 cm^{-1}) of UiO-67-CH_3; spectral broadening and reduction in intensity by 473 K (Figure S6). Upon cooling, the ν(N–H) and ν(C–H) bands of UiO-67-NH_2 and UiO-67-CH_3, respectively, sharpen and return to their initial states, indicating that the thermally induced response is fully reversible (Figures 5 and S6). It is worth stating that the changes detected in the IR are not because of loss of material as no product evolution is observed from the TPD for temperatures below 473 K, as discussed in detail later.

Irreversible Thermal Effects. All UiO-67 MOFs undergo three stages of changes before their final degradation at around 800 K, as revealed by *in situ* PXRD recorded while samples are heated from 300 to 900 K (Figures 6, S22–S24). It is important to note that unlike the IR or TPD experiments, XRD samples were not activated prior to the thermal degradation experiments. As a result, the first stage of change reflects a desolvation process up to 450 K, indicated by the change of several low 2θ angle peaks, for example, the disappearance of the peak at 3.3° (Figures S22–S24). There is very little peak shifting, showing that the rigidity of the

https://dx.doi.org/10.1021/acs.chemmater.0c03889
Chem. Mater. 2021, 33, 910–920

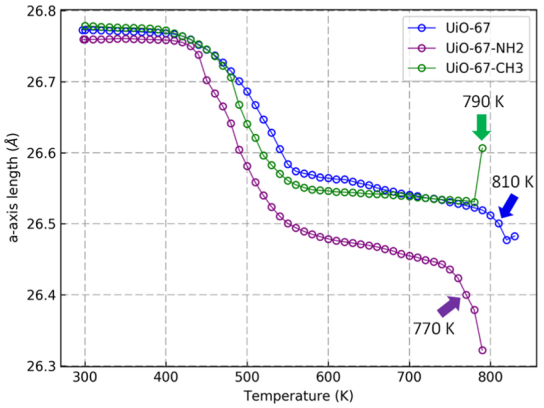

Figure 6. Unit cell edge lengths (Å) of the UiO-67 MOFs as samples are heated from 300 to 900 K during the thermal degradation experiment. Degradation temperatures (K) are marked with arrows. The associated error in *a*-axis length (Å) is smaller than the symbol size.

frameworks is not affected by the removal of residual solvent molecules. Starting from the end of the desolvation stage, the MOFs display significant lattice contraction from 420 to 550 K, where all XRD peaks shift to higher angles without apparent change of relative intensities. The lattice contraction at around 480 K in the temperature cycling experiment is in fact part of the second stage revealed here. From 550 K to the point of degradation, the lattice contraction continues, reminiscent of the NTE reported above. UiO-67-CH_3 has the lowest contraction rate among the three MOFs, which is consistent with the observation in the temperature cycling experiments (Table 1).

In addition to the multistage lattice contraction, other structural changes occurring to UiO-67 in the degradation process are revealed from the *in situ* XRD data. The refined site occupancy of the μ_3-O (H) site, which is 1 for the starting material, starts decreasing at 480 K and reaches 0.78(2) at 580 K (Figure S26). Meanwhile, the average bond length between Zr and μ_3-O (H) decreases from 2.14(1) to 2.10(1) Å (Figure S26). These results support the dehydroxylation model, proposed based on computation and X-ray absorption spectroscopy (XAS) studies of UiO-66 and UiO-67 in which the $Zr_6O_4(OH)_4$ node transforms to a distorted Zr_6O_6 node,[15,23] which in theory would bring the μ_3-O (H) site occupancy from 1 to 0.75 and shorten the average Zr to μ_3-O (H) distance as the hydroxyls are removed.

Dehydroxylation of the Zr node is the structural reason for the second stage of the lattice contraction shown in Figure 6. This process is also accompanied by a drastic increase of the Zr ADP (Figure S27), indicating that the Zr atoms in the Zr_6O_6 node are locally deviated from the Zr site position in the structure model which assumes an ideal octahedral shape for the Zr_6 node. The local distortion of the Zr_6O_6 node is difficult to model with XRD, which probes the global crystal structure. In other studies using techniques sensitive to local structures, such as XAS and with X-ray pair distribution function analysis, a split of the Zr−Zr edge distance from an ideal octahedron was evidenced.[15,24]

Irreversible structural changes induced by heating are also identified in the MOF IR spectral signature as the sample temperature is increased beyond the temperature of activation (>473 K). It should be noted that we define irreversible change as the loss of material originating from the degradation of the MOF. For UiO-67, the first and most prominent spectral change during heating from 300 to 1273 K is the gradual loss in signal intensity at 3678 cm^{-1} and is recognized as the removal of the bridging μ_3-OH groups from the zirconium clusters, or dehydroxylation (Figure 7a). Additionally, we observe perturbations of MOF skeletal modes below 800 cm^{-1} during the dehydroxylation process (Figure 7b). This region is rich with spectral features associated with a variety of Zr−O modes coupled with C−H and O−H bending modes.[15] During heating, a peak at 770 cm^{-1} grows in intensity while bands at 752, 736, and 702 cm^{-1} disappear. Moreover, the loss of a feature at 673 cm^{-1} is accompanied by the appearance of two new bands at 647 and 638 cm^{-1} (Figure 7b). Such substantial changes in this region suggest a loss of local symmetry at the node, most likely associated with the structural transition from the fully hydroxylated, $Zr_6O_4(OH)_4$, to the fully dehydroxylated Zr_6O_6 node.[15,30,45]

The transition to the fully dehydroxylated node has been reported to increase the strength of carboxylate binding to the zirconia metal centers for the isoreticular analogues, UiO-66 and UiO-66-NH_2, as evidenced by a blueshift and broadening in carboxylate modes upon thermal treatment.[45] However, in the present study, the removal of hydroxyl groups correlates

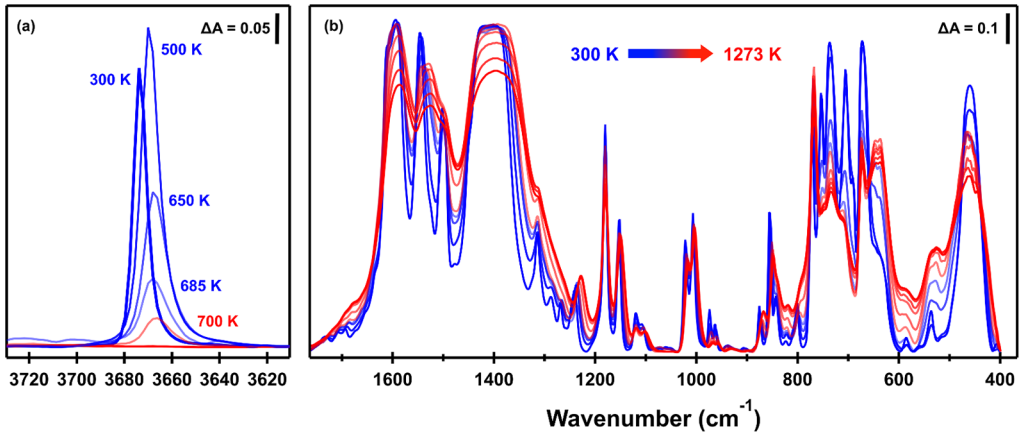

Figure 7. IR spectra recorded during heating from 300 to 1273 K for UiO-67 showing the temperature-dependent spectral changes for (a) $\nu(OH)_{free}$ at 3678 cm^{-1} and (b) MOF skeletal modes between 1750 and 400 cm^{-1}. All baseline corrected spectra are presented for increasing temperature from blue to red, as indicated by the color legend.

https://dx.doi.org/10.1021/acs.chemmater.0c03889
Chem. Mater. 2021, 33, 910−920

with a redshift and broadening of the broad carboxylate modes centered at 1409 and 1595 cm^{-1} in the baseline corrected spectra for UiO-67 (Figure 7b), suggesting a weakening carboxylate node binding in the absence of O−H groups, which may be associated with thermally induced changes in the dihedral angle of the biphenyl linker of UiO-67. Similar behavior was observed for the coordinated $\nu(COO^-)$ modes of UiO-67-NH_2 and UiO-67-CH_3 (Figure S7).

The dehydroxylation is also evidenced by the decrease of the μ_3-O (H) site occupancy from our XRD refinement results described above. In fact, the calculated IR spectra reported by Valenzano *et al.*,[15] comparing the IR signature of the hydroxylated *versus* dehydroxylated material, describe that the removal of bridging μ_3-OH groups results in significant structural distortions, reflected in a large blueshift (~57 cm^{-1}) in the μ_3-O stretching frequency (reported at 673 cm^{-1} for the hydroxylated material), and the disappearance of the (OH)−Zr−(OH) bending mode (reported at 470 cm^{-1}).[15] Indeed, a plot of the normalized IR intensity as a function of temperature reveals that the disappearance of the μ_3-O stretch (673 cm^{-1}) coincides with the onset of the loss of the free hydroxyls (3678 cm^{-1}) and supports the transition to the dehydroxylated material (Figure S8).

The onset of significant loss of μ_3-OH groups is recognized by tracking the normalized absorbance as a function of temperature, as shown for UiO-67 in Figure 8. Similar IR

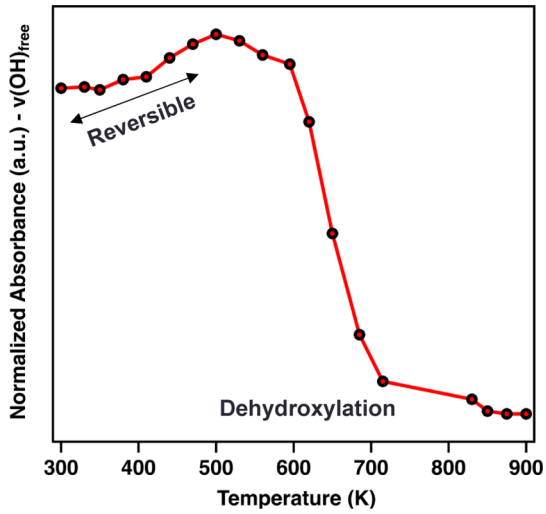

Figure 8. Normalized IR intensity of the μ_3-OH peak for UiO-67 during heating from 300 K to the point of complete dehydroxylation (~900 K).

profiles for UiO-67-NH_2 and UiO-67-CH_3 are given in Figure S9. As discussed previously, our IR results indicate that all UiO-67 MOFs undergo reversible thermal behavior when heated up to the activation temperature (473 K). From Figure 8, continued heating above 473 K leads to a significant loss of $\nu(OH)_{free}$, signaling the onset of node dehydroxylation. For UiO-67, dehydroxylation is initiated at ~500 K, while the onset for UiO-67-CH_3 (450 K) and UiO-67-NH_2 (430 K) occurs at lower temperatures (Figure S9). The lower onset temperature is likely reflective of the higher degree of structural disorder and higher degree of defect generation during the heating of the functionalized samples. The trend of decreasing dehydroxylation onset temperature from the unfunctionalized to the functionalized UiO-67 is in agreement with the XRD results (Figure 6).

TPD-MS provides information on mass loss, thermal stability, and processes occurring *in situ* as the UiO-67 MOFs are heated from 300 K to the point of degradation. As samples are heated under vacuum, desorption will occur when molecules gain enough energy to overcome the activation barrier and are removed from the MOF as gaseous products, which are then analyzed by the quadruple mass spectrometer. It should be noted that during heating from 300 to 1273 K, we observe no release of material from the TPD profile for temperatures below 473 K. However, as sample temperatures exceed 473 K, the evolution of MS signals from water (m/z = 18, H_2O^+), CO_2 (m/z = 44, CO_2^+), and CO (m/z = 28, CO^+) is identified, which strongly indicates irreversible structural change (Figure 9).

At 300 K, all UiO-67 MOFs are fully hydroxylated, evident by the presence of free bridging hydroxyl groups (3678 cm^{-1}) in the IR spectra (Figures 1, S1 and S2). In the TPD profiles, the evolution of H_2O (m/z = 18) is attributed to the loss of O−H as water, resulting from the dehydroxylation of the Zr node. It is clear that functionalization of the organic linker influences the dehydroxylation process. For UiO-67 (Figure 9a) and UiO-67-NH_2 (Figure 9b), the evolution of H_2O (m/z = 18) is initiated at ~500 K, while for the methyl-functionalized material, the onset temperature of dehydroxylation (480 K) is notably lower (Figure 9c). This is likely related to a higher percentage of defects and thus higher degree of structural disorder for UiO-67-CH_3 observed by XRD. Moreover, while the onset temperature for dehydroxylation is similar for UiO-67 and UiO-67-NH_2, the TPD-MS line-shapes are notably different, where a broader band distribution and a high temperature shoulder at 700 K are observed for UiO-67-NH_2 (Figure 9b), suggesting that functionalization of the linker with the polar $-NH_2$ group allows for stronger binding of O−H on the node possibly *via* inductive effects.

Previous thermogravimetry studies of UiO-type MOFs report CO_2 and benzene fragments as the primary decomposition products arising from the detachment of the linker from the Zr node. Indeed, as the sample temperature increases beyond 700 K, a growth in MS signal intensity is observed for CO_2^+ (m/z = 44) and provides evidence for decarboxylation of the organic linker, likely *via* cleavage of Zr−OC bonds at the 4 and 4′ position of the dicarboxylic acid linker, followed by cleavage of aromatic−C bonds to release CO_2, as illustrated by the schematic in Figure 10.

The onset of decarboxylation is first observed for the functionalized UiO-67 MOFs at ~650 K (Figure 9b,c), whereas the evolution of the CO_2^+ MS signal is not observed until temperatures approach 875 K for unfunctionalized UiO-67 (Figure 9a). These results indicate that linker functionalization reduces the thermal stability in UiO-67 MOFs. A similar finding has been reported for the thermolysis of the organic linker from multivariate UiO-66 MOFs, where TGA−MS experiments, performed in air, revealed that functionalization of the benzene−dicarboxylate linker with NH_2 groups reduces the onset decomposition temperature from 753 to 573 K.[46] Additionally, the position of substituents on the linker is reported to play a key role during the degradation of UiO MOFs.[11] Upon decarboxylation, substituent groups located closer to the inorganic node (*i.e.*, ortho to carboxylate groups of the linker) reportedly satisfy the loss in coordination, resulting in local distortions in coordination of the node,

https://dx.doi.org/10.1021/acs.chemmater.0c03889
Chem. Mater. 2021, 33, 910−920

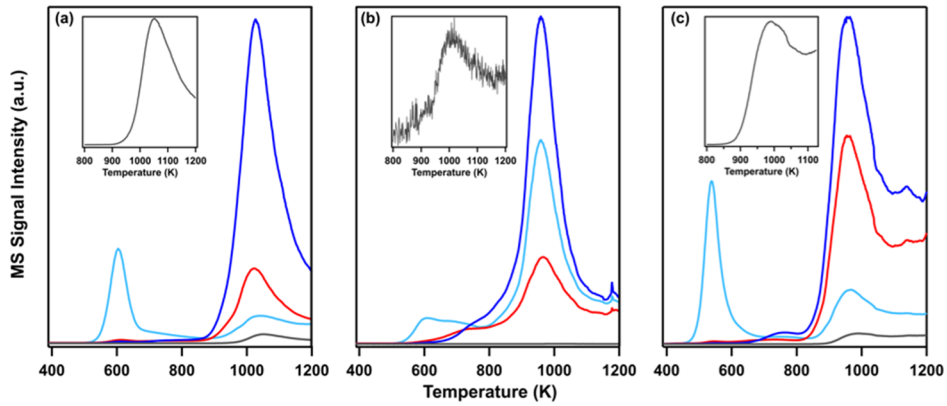

Figure 9. TPD-MS profiles of (a) UiO-67, (b) UiO-67-NH_2, and (c) UiO-67-CH_3 acquired during continuous heating at 2 K/s from 300 to 1273 K tracking mass fragments m/z = 18 (H_2O^+, teal), m/z = 28 (CO^+, red), m/z = 44 (CO_2^+, blue), and m/z = 76 ($(C_{12}H_8)^{2+}$, gray) or 83 ($(C_{12}H_7X)^{2+}$ for UiO-67-NH_2 and UiO-67-CH_3, gray).

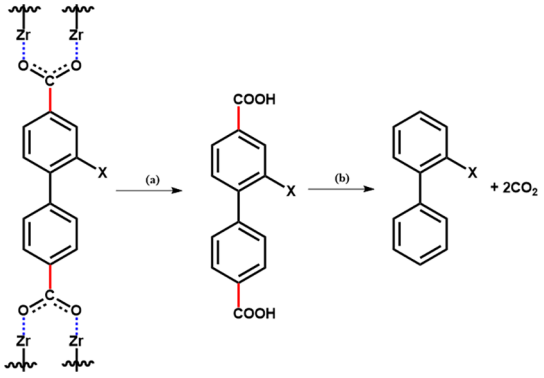

Figure 10. Schematic representation of linker degradation in UiO-67 MOFs, where X represents −H, −NH_2, or −CH_3 groups for UiO-67, UiO-67-NH_2, and UiO-67-CH_3, respectively. Degradation proceeds *via* (a) cleavage of Zr−OC bonds (blue, dashed) followed by (b) cleavage of the aromatic-C bonds to release CO_2, leaving behind the residual linker fragment.

ultimately destabilizing the overall framework and significantly lowering the thermal stability in comparison to the unfunctionalized MOFs. However, the decomposition temperatures of UiO MOFs with substituent meta to carboxylate groups of the linker were lower compared to unfunctionalized MOFs but higher than ortho-functionalized MOFs.[11] This result supports the observations in our study where the functionalized UiO-67 samples possessing amine and methyl substituents, respectively, that are meta to the carboxylate groups of the linker exhibit only slightly lower decomposition temperatures compared to unfunctionalized UiO-67. Moreover, the evolution of the CO_2^+ MS signals coincides with a high temperature m/z = 18 signal within the same temperature range, indicating complete degradation of the BPDC linkers.

Unlike previous reports, we also observe the evolution of CO^+ (m/z = 28) during the heating process. The CO_2^+ (m/z = 44) and CO^+ (m/z = 28) fragments for UiO-67 and UiO-67-CH_3 produced similar temperature profiles (Figure S10), indicating that UiO-67 and UiO-67-CH_3 share similar CO_2 release processes during thermal degradation. Moreover, for these MOFs, it seems likely that CO_2 is a major decomposition product. However, we note that for UiO-67-CH_3, the relative intensity of CO^+ is much greater than that for UiO-67. From our previous study, and as described in the Experimental section, it was determined that all UiO-67 MOFs reported here possess missing linker defects; on average less than or equal to one missing linker for UiO-67 and UiO-67-NH_2 and 1.6 missing linkers per SBU for UiO-67-CH_3.[35] It is possible that some contribution of CO in the degradation products for UiO-67-CH_3 could originate from dangling carboxylate groups from imperfectly coordinated BPDC linkers (*e.g.*, monodentate or uncoordinated BPDC) or formate capping groups bound to the Zr node.[47]

Decarboxylation of UiO-67-NH_2 is uniquely different from UiO-67 and UiO-67-CH_3. While the temperature profiles of the CO_2^+ and CO^+ fragments track each other for UiO-67 and UiO-67-CH_3, they do not for the aminated MOF (inset, Figure S10), where two CO^+ MS signals are observed and is substantially broader than the CO_2^+ MS signal. This suggests that UiO-67-NH_2 may follow a different CO_2 release process compared to UiO-67 and UiO-67-CH_3. This hypothesis has been recently reported by Healy *et al.*,[11] after the review of TGA−MS data for UiO-67 and UiO-67-NH_2 acquired during the thermal degradation process.[32] While the mechanism of CO_2 release remains unclear for UiO-67-NH_2, our results support previous observations and we anticipate that the difference between the CO_2 release processes to be related to structural defects.

Immediately following linker decarboxylation, we observe the formation of a doubly ionized linker fragment, that is, with 2 units of positive charge, specifically: m/z = 76 (UiO-67) and m/z = 83 (UiO-67-NH_2, UiO-67-CH_3), as illustrated in Figure 10. The associated TPD-MS signals are provided for each MOF in the inset of Figure 9. The onset of MS signal detection of the residual linker fragments is observed at lower temperatures for UiO-67-CH_3 (850 K) and UiO-67-NH_2 (900 K) compared to UiO-67 (925 K). No significant fragmentation of the linker was observed during heating, suggesting that the BPDC linker detaches as a complete unit. This observation is in accordance with the mechanism reported by Cavka *et al.*,[30] for the decomposition of UiO-66, where the TGA−MS signal associated with the benzene fragment was observed at ∼800 K. However, the authors were unable to clearly identify whether benzene and CO_2 were primary or secondary fragments of decomposition, which made the mechanism of decomposition unclear. We observed that the evolution of the residual linker fragments (inset, Figure 9) follows the evolution of CO (m/z = 28) and CO_2 (m/z = 44), suggesting that the primary process during framework decomposition is the weakening of Zr−OC bonds and

https://dx.doi.org/10.1021/acs.chemmater.0c03889
Chem. Mater. 2021, 33, 910−920

sequential loss of CO_2 and linker fragments. This is further supported by the loss of IR signals for the functional groups, ring and carboxylate modes at similar temperatures.

The observed decomposition temperatures in our studies are higher than the reported degradation temperatures of UiO series MOFs, as evaluated using TGA−MS experiments performed under inert and ambient environments, and suggest that the environmental conditions may play a significant role in thermal stability.[30,32,48,49] For example, the thermal decomposition temperature for UiO-67 was found to be ∼673 K for TGA−MS experiments conducted in the presence of oxygen (*e.g.*, ambient or under O_2 flow),[32,50] while under an inert nitrogen environment, the thermal stability is increased to ∼723 K.[30,49] It appears that MOF stability is increased in the absence of oxygen and is in good agreement with our current study, which reports that thermal decomposition temperatures are greater than 723 K for all UiO-67 MOFs under UHV conditions. The overall stability trend of UiO-67 MOFs reveals that functionalization decreases the MOF thermal stability as: UiO-67 > UiO-67-CH_3 > UiO-67-NH_2. We emphasize that, in this study, we report for the first time the thermal decomposition temperature for UiO-67-CH_3. Until now, the decomposition for only UiO-67-$(CH_3)_2$ has been reported.[48] When the MOFs are heated under UHV conditions, the decomposition products generated *in situ* are continuously evacuated, removing any interference from residual ambient (O_2) and/or carrier gases (N_2/Ar) which can contribute to the degradation process. Ultimately, UHV environments may provide increased thermal stability to monitor thermal degradation events.

CONCLUSIONS

We have provided a comprehensive evaluation of the temperature-dependent structural changes which influence the thermal stability of UiO-67 and its functional analogues, UiO-67-NH_2 and UiO-67-CH_3. For the first time, we have correlated structural dynamics of the UiO-67 MOFs to rich, reversible thermal behavior observed though temperature-programmed IR spectroscopy and identified the distortion of the carboxylate group as the structural origin of the NTE. The pendant groups on the functionalized linkers of UiO-67-NH_2 and UiO-67-CH_3 are uniquely affected by temperature, highlighting the importance of critically evaluating temperature-dependent MOF spectral features. This finding provides a basis whereby future studies can distinguish temperature dependent interactions of MOFs with guest molecules from effects intrinsic to the heating of the MOFs.

Activated UiO-67 materials undergo two stages of irreversible change, which are intimately tied to Zr node deformation resulting from loss of OH species and the isotropic NTE behavior of these UiO-67 MOFs. The initial and substantial lattice contraction observed by XRD between 420 and 550 K are in excellent agreement with IR and MS results, signaling the onset of dehydroxylation resulting in defect generation and subsequent node distortion. As temperatures are increased beyond 550 K, the second stage of lattice contraction is related to the NTE of the dehydroxylated structure.

We emphasize that this study reports, for the first time, the thermal decomposition temperature of UiO-67-CH_3. Our studies confirm that in the absence of oxygen and under UHV conditions, thermal stability of UiO-67 MOFs is increased, releasing mainly carbon dioxide and water as primary degradation products. The overall stability trend of UiO-67 MOFs reveals that functionalization decreases the MOF thermal stability as: UiO-67 > UiO-67-CH_3 > UiO-67-NH_2. Previous literature reports a wide temperature range (673−723 K) for the thermal decomposition of UiO-67, which indicates that there is likely an environmental dependence on MOF thermal stability. However, it remains clear that the thermal stability of the unfunctionalized material is greater than the functionalized analogues, arising from the linker thermolysis. The correlation between IR, MS, and PXRD studies provides a real-time understanding of the thermal events that occur when UiO-67 MOFs are heated up to 1273 K. UHV environments are found to increase the range of thermal stability, allowing for an in-depth quantitative understanding of the intrinsic processes that govern the breakdown of these MOFs and provide guidance for UiO-67 MOF use in diverse applications.

ASSOCIATED CONTENT

Supporting Information

The Supporting Information is available free of charge at https://pubs.acs.org/doi/10.1021/acs.chemmater.0c03889.

Experimental PXRD methods, characterization of the MOF structures by IR and XRD, and detailed XRD analysis procedure (PDF)

PXRD refined structures (CIF)

AUTHOR INFORMATION

Corresponding Authors

Wenqian Xu − *X-ray Science Division, Advanced Photon Source, Argonne National Laboratory, Lemont, Illinois 60439, United States;* orcid.org/0000-0002-4815-6253; Email: wenqianxu@anl.gov

Eric Borguet − *Department of Chemistry, Temple University, Philadelphia, Pennsylvania 19122, United States;* orcid.org/0000-0003-0593-952X; Email: eborguet@temple.edu

Authors

Isabella Goodenough − *Department of Chemistry, Temple University, Philadelphia, Pennsylvania 19122, United States;* orcid.org/0000-0001-8581-4473

Venkata Swaroopa Datta Devulapalli − *Department of Chemistry, Temple University, Philadelphia, Pennsylvania 19122, United States;* orcid.org/0000-0003-1860-9888

Mikaela C. Boyanich − *Department of Chemistry, Temple University, Philadelphia, Pennsylvania 19122, United States;* orcid.org/0000-0002-7109-0993

Tian-Yi Luo − *Department of Chemistry, University of Pittsburgh, Pittsburgh, Pennsylvania 15260, United States;* orcid.org/0000-0002-9973-9328

Mattheus De Souza − *Department of Chemistry, University of Pittsburgh, Pittsburgh, Pennsylvania 15260, United States;* orcid.org/0000-0002-2057-3610

Mélissandre Richard − *Department of Chemistry, Temple University, Philadelphia, Pennsylvania 19122, United States;* orcid.org/0000-0001-6789-6997

Nathaniel L. Rosi − *Department of Chemistry, University of Pittsburgh, Pittsburgh, Pennsylvania 15260, United States;* orcid.org/0000-0001-8025-8906

Complete contact information is available at: https://pubs.acs.org/10.1021/acs.chemmater.0c03889

https://dx.doi.org/10.1021/acs.chemmater.0c03889
Chem. Mater. 2021, 33, 910−920

Notes

The authors declare no competing financial interest.

■ ACKNOWLEDGMENTS

The authors thank Avery Green and Carl Ventrice for providing LabVIEW code to run TPD experiments. This project received support from the Defense Threat Reduction Agency (DTRA) (grant no. HDTRA1-16-1-0044). This research used resources of the Advanced Photon Source, a U.S. Department of Energy (DOE) Office of Science User Facility operated for the DOE Office of Science by ANL under contract no. DE-AC02-06CH11357.

■ REFERENCES

(1) Li, J.-R.; Kuppler, R. J.; Zhou, H.-C. Selective Gas Adsorption and Separation in Metal-Organic Frameworks. *Chem. Soc. Rev.* **2009**, *38*, 1477−1504.

(2) Li, B.; Wen, H.-M.; Zhou, W.; Chen, B. Porous Metal-Organic Frameworks for Gas Storage and Separation: What, How, and Why? *J. Phys. Chem. Lett.* **2014**, *5*, 3468−3479.

(3) Kreno, L. E.; Leong, K.; Farha, O. K.; Allendorf, M.; Van Duyne, R. P.; Hupp, J. T. Metal-Organic Framework Materials as Chemical Sensors. *Chem. Rev.* **2012**, *112*, 1105−1125.

(4) Li, Y.-A.; Zhao, C.-W.; Zhu, N.-X.; Liu, Q.-K.; Chen, G.-J.; Liu, J.-B.; Zhao, X.-D.; Ma, J.-P.; Zhang, S.; Dong, Y.-B. Nanoscale UiO-MOF-Based Luminescent Sensors for Highly Selective Detection of Cysteine and Glutathione and Their Application in Bioimaging. *Chem. Commun.* **2015**, *51*, 17672−17675.

(5) Yang, D.; Odoh, S. O.; Borycz, J.; Wang, T. C.; Farha, O. K.; Hupp, J. T.; Cramer, C. J.; Gagliardi, L.; Gates, B. C. Tuning Zr_6 Metal-Organic Framework (MOF) Nodes as Catalyst Supports: Site Densities and Electron-Donor Properties Influence Molecular Iridium Complexes as Ethylene Conversion Catalysts. *ACS Catal.* **2016**, *6*, 235−247.

(6) Tanabe, K. K.; Cohen, S. M. Postsynthetic Modification of Metal-Organic Frameworks-a Progress Report. *Chem. Soc. Rev.* **2011**, *40*, 498−519.

(7) Li, N.; Xu, J.; Feng, R.; Hu, T.-L.; Bu, X.-H. Governing Metal-Organic Frameworks Towards High Stability. *Chem. Commun.* **2016**, *52*, 8501−8513.

(8) Howarth, A. J.; Liu, Y. Y.; Li, P.; Li, Z. Y.; Wang, T. C.; Hupp, J.; Farha, O. K. Chemical, thermal and mechanical stabilities of metal-organic frameworks. *Nat. Rev. Mater.* **2016**, *1*, 15018.

(9) Furukawa, H.; Cordova, K. E.; O'Keeffe, M.; Yaghi, O. M. The Chemistry and Applications of Metal-Organic Frameworks. *Science* **2013**, *341*, 1230444.

(10) Cheetham, A. K.; Rao, C. N. R.; Feller, R. K. Structural Diversity and Chemical Trends in Hybrid Inorganic-Organic Framework Materials. *Chem. Commun.* **2006**, *46*, 4780−4795.

(11) Healy, C.; Patil, K. M.; Wilson, B. H.; Hermanspahn, L.; Harvey-Reid, N. C.; Howard, B. I.; Kleinjan, C.; Kolien, J.; Payet, F.; Telfer, S. G.; Kruger, P. E.; Bennett, T. D. The Thermal Stability of Metal-Organic Frameworks. *Coord. Chem. Rev.* **2020**, *419*, 213388.

(12) Coudert, F.-X. Responsive Metal-Organic Frameworks and Framework Materials: Under Pressure, Taking the Heat, in the Spotlight, with Friends. *Chem. Mater.* **2015**, *27*, 1905−1916.

(13) Mouchaham, G.; Wang, S.; Serre, C. The Stability of Metal−Organic Frameworks. In *Metal-Organic Frameworks: Applications in Separations and Catalysis*, 1st ed.; García, H.; Navalón, S., Eds.; Wiley-VCH Verlag GmbH & Co. KGaA, 2018, p 14.

(14) DeCoste, J. B.; Peterson, G. W.; Jasuja, H.; Glover, T. G.; Huang, Y.-g.; Walton, K. S. Stability and Degradation Mechanisms of Metal-Organic Frameworks Containing the $Zr_6O_4(OH)_4$ Secondary Building Unit. *J. Mater. Chem. A* **2013**, *1*, 5642−5650.

(15) Valenzano, L.; Civalleri, B.; Chavan, S.; Bordiga, S.; Nilsen, M. H.; Jakobsen, S.; Lillerud, K. P.; Lamberti, C. Disclosing the Complex Structure of UiO-66 Metal Organic Framework: A Synergic Combination of Experiment and Theory. *Chem. Mater.* **2011**, *23*, 1700−1718.

(16) Chavan, S.; Vitillo, J. G.; Gianolio, D.; Zavorotynska, O.; Civalleri, B.; Jakobsen, S.; Nilsen, M. H.; Valenzano, L.; Lamberti, C.; Lillerud, K. P.; Bordiga, S. H_2 Storage in Isostructural UiO-67 and UiO-66 MOFs. *Phys. Chem. Chem. Phys.* **2012**, *14*, 1614−1626.

(17) Van de Voorde, B.; Stassen, I.; Bueken, B.; Vermoortele, F.; De Vos, D.; Ameloot, R.; Tan, J.-C.; Bennett, T. D. Improving the Mechanical Stability of Zirconium-based Metal-Organic Frameworks by Incorporation of Acidic Modulators. *J. Mater. Chem. A* **2015**, *3*, 1737−1742.

(18) Wu, H.; Yildirim, T.; Zhou, W. Exceptional Mechanical Stability of Highly Porous Zirconium Metal-Organic Framework UiO-66 and Its Important Implications. *J. Phys. Chem. Lett.* **2013**, *4*, 925−930.

(19) Zhang, W.; Maul, J.; Vulpe, D.; Moghadam, P. Z.; Fairen-Jimenez, D.; Mittleman, D. M.; Zeitler, J. A.; Erba, A.; Ruggiero, M. T. Probing the Mechanochemistry of Metal-Organic Frameworks with Low-Frequency Vibrational Spectroscopy. *J. Phys. Chem. C* **2018**, *122*, 27442−27450.

(20) Kalidindi, S. B.; Nayak, S.; Briggs, M. E.; Jansat, S.; Katsoulidis, A. P.; Miller, G. J.; Warren, J. E.; Antypov, D.; Corà, F.; Slater, B.; Prestly, M. R.; Martí-Gastaldo, C.; Rosseinsky, M. J. Chemical and Structural Stability of Zirconium-based Metal-Organic Frameworks with Large Three-Dimensional Pores by Linker Engineering. *Angew. Chem., Int. Ed.* **2015**, *54*, 221−226.

(21) Rogge, S. M. J.; Wieme, J.; Vanduyfhuys, L.; Vandenbrande, S.; Maurin, G.; Verstraelen, T.; Waroquier, M.; Van Speybroeck, V. Thermodynamic Insight in the High-Pressure Behavior of UiO-66: Effect of Linker Defects and Linker Expansion. *Chem. Mater.* **2016**, *28*, 5721−5732.

(22) Gutov, O. V.; Bury, W.; Gomez-Gualdron, D. A.; Krungleviciute, V.; Fairen-Jimenez, D.; Mondloch, J. E.; Sarjeant, A. A.; Al-Juaid, S. S.; Snurr, R. Q.; Hupp, J. T.; Yildirim, T.; Farha, O. K. Water-Stable Zirconium-Based Metal-Organic Framework Material with High-Surface Area and Gas-Storage Capacities. *Chem.—Eur. J.* **2014**, *20*, 12389−12393.

(23) Shearer, G. C.; Forselv, S.; Chavan, S.; Bordiga, S.; Mathisen, K.; Bjørgen, M.; Svelle, S.; Lillerud, K. P. In Situ Infrared Spectroscopic and Gravimetric Characterisation of the Solvent Removal and Dehydroxylation of the Metal Organic Frameworks UiO-66 and UiO-67. *Top. Catal.* **2013**, *56*, 770−782.

(24) Platero-Prats, A. E.; Mavrandonakis, A.; Gallington, L. C.; Liu, Y.; Hupp, J. T.; Farha, O. K.; Cramer, C. J.; Chapman, K. W. Structural Transitions of the Metal-Oxide Nodes within Metal-Organic Frameworks: On the Local Structures of NU-1000 and UiO-66. *J. Am. Chem. Soc.* **2016**, *138*, 4178−4185.

(25) Zhou, W.; Wu, H.; Yildirim, T.; Simpson, J. R.; Walker, A. R. H. Origin of the Exceptional Negative Thermal Expansion in Metal-Organic Framework-5 Zn_4O(1,4-benzenedicarboxylate)$_3$. *Phys. Rev. B* **2008**, *78*, 054114.

(26) Wu, Y.; Kobayashi, A.; Halder, G. J.; Peterson, V. K.; Chapman, K. W.; Lock, N.; Southon, P. D.; Kepert, C. J. Negative Thermal Expansion in the Metal-Organic Framework Material Cu_3(1,3,5-benzenetricarboxylate)$_2$. *Angew. Chem., Int. Ed.* **2008**, *47*, 8929−8932.

(27) Burtch, N. C.; Baxter, S. J.; Heinen, J.; Bird, A.; Schneemann, A.; Dubbeldam, D.; Wilkinson, A. P. Negative Thermal Expansion Design Strategies in a Diverse Series of Metal-Organic Frameworks. *Adv. Funct. Mater.* **2019**, *29*, 1904669.

(28) du Bourg, L. B.; Ortiz, A. U.; Boutin, A.; Coudert, F. X. Thermal and Mechanical Stability of Zeolitic Imidazolate Frameworks Polymorphs. *APL Mater.* **2014**, *2*, 124110.

(29) Cliffe, M. J.; Hill, J. A.; Murray, C. A.; Coudert, F.-X.; Goodwin, A. L. Defect-dependent Colossal Negative Thermal Expansion in UiO-66(Hf) Metal-Organic Framework. *Phys. Chem. Chem. Phys.* **2015**, *17*, 11586−11592.

(30) Cavka, J. H.; Jakobsen, S.; Olsbye, U.; Guillou, N.; Lamberti, C.; Bordiga, S.; Lillerud, K. P. A New Zirconium Inorganic Building

Brick Forming Metal Organic Frameworks with Exceptional Stability. *J. Am. Chem. Soc.* **2008**, *130*, 13850−13851.
(31) Perfecto-Irigaray, M.; Beobide, G.; Castillo, O.; da Silva, I.; García-Lojo, D.; Luque, A.; Mendia, A.; Pérez-Yáñez, S. $[Zr_6O_4(OH)_4(benzene\text{-}1,4\text{-}dicarboxylato)_6]_n$: A Hexagonal Polymorph of UiO-66. *Chem. Commun.* **2019**, *55*, 5954−5957.
(32) Tian, C.; Zhao, J.; Ou, X.; Wan, J.; Cai, Y.; Lin, Z.; Dang, Z.; Xing, B. Enhanced Adsorption of p-Arsanilic Acid from Water by Amine-Modified UiO-67 as Examined Using Extended X-ray Absorption Fine Structure, X-ray Photoelectron Spectroscopy, and Density Functional Theory Calculations. *Environ. Sci. Technol.* **2018**, *52*, 3466−3475.
(33) Kazachkin, D. V.; Nishimura, Y.; Witek, H. A.; Irle, S.; Borguet, E. Dramatic Reduction of IR Vibrational Cross Sections of Molecules Encapsulated in Carbon Nanotubes. *J. Am. Chem. Soc.* **2011**, *133*, 8191−8198.
(34) Feng, X.; Matranga, C.; Vidic, R.; Borguet, E. A Vibrational Spectroscopic Study of the Fate of Oxygen-containing Functional Groups and Trapped CO_2 in Single-Walled Carbon Nanotubes During Thermal Treatment. *J. Phys. Chem. B* **2004**, *108*, 19949−19954.
(35) Ruffley, J. P.; Goodenough, I.; Luo, T.-Y.; Richard, M.; Borguet, E.; Rosi, N. L.; Johnson, J. K. Design, Synthesis, and Characterization of Metal-Organic Frameworks for Enhanced Sorption of Chemical Warfare Agent Simulants. *J. Phys. Chem. C* **2019**, *123*, 19748−19758.
(36) Kwon, S.; Vidic, R.; Borguet, E. The Effect of Surface Chemical Functional Groups on the Adsorption and Desorption of a Polar Molecule, Acetone, from a Model Carbonaceous Surface, Graphite. *Surf. Sci.* **2003**, *522*, 17−26.
(37) Toby, B. H.; Von Dreele, R. B. GSAS-II: The Genesis of a Modern Open-source All Purpose Crystallography Software Package. *J. Appl. Crystallogr.* **2013**, *46*, 544−549.
(38) Plonka, A. M.; Wang, Q.; Gordon, W. O.; Balboa, A.; Troya, D.; Guo, W.; Sharp, C. H.; Senanayake, S. D.; Morris, J. R.; Hill, C. L.; Frenkel, A. I. In Situ Probes of Capture and Decomposition of Chemical Warfare Agent Simulants by Zr-Based Metal Organic Frameworks. *J. Am. Chem. Soc.* **2017**, *139*, 599−602.
(39) Wang, G.; Sharp, C.; Plonka, A. M.; Wang, Q.; Frenkel, A. I.; Guo, W.; Hill, C.; Smith, C.; Kollar, J.; Troya, D.; Morris, J. R. Mechanism and Kinetics for Reaction of the Chemical Warfare Agent Simulant, DMMP(g), with Zirconium(IV) MOFs: An Ultrahigh-Vacuum and DFT Study. *J. Phys. Chem. C* **2017**, *121*, 11261−11272.
(40) Ren, J.; Ledwaba, M.; Musyoka, N. M.; Langmi, H. W.; Mathe, M.; Liao, S.; Pang, W. Structural Defects in Metal-Organic Frameworks (MOFs): Formation, Detection and Control Towards Practices of Interests. *Coord. Chem. Rev.* **2017**, *349*, 169−197.
(41) Kandiah, M.; Nilsen, M. H.; Usseglio, S.; Jakobsen, S.; Olsbye, U.; Tilset, M.; Larabi, C.; Quadrelli, E. A.; Bonino, F.; Lillerud, K. P. Synthesis and Stability of Tagged UiO-66 Zr-MOFs. *Chem. Mater.* **2010**, *22*, 6632−6640.
(42) Huang, Y.; Qin, W.; Li, Z.; Li, Y. Enhanced Stability and CO_2 Affinity of a UiO-66 Type Metal-Organic Framework Decorated with Dimethyl Groups. *Dalton Trans.* **2012**, *41*, 9283−9285.
(43) Ragon, F.; Campo, B.; Yang, Q.; Martineau, C.; Wiersum, A. D.; Lago, A.; Guillerm, V.; Hemsley, C.; Eubank, J. F.; Vishnuvarthan, M.; Taulelle, F.; Horcajada, P.; Vimont, A.; Llewellyn, P. L.; Daturi, M.; Devautour-Vinot, S.; Maurin, G.; Serre, C.; Devic, T.; Clet, G. Acid-functionalized UiO-66(Zr) MOFs and their Evolution After Intra-framework Cross-linking: Structural Features and Sorption Properties. *J. Mater. Chem. A* **2015**, *3*, 3294−3309.
(44) Nakamoto, K. Applications in Organometallic Chemistry. In *Infrared and Raman Spectra of Inorganic and Coordination Compounds*, 6th ed.; Wiley: Hoboken, N.J., 2008, pp 275−331.
(45) Lemaire, P. C.; Lee, D. T.; Zhao, J.; Parsons, G. N. Reversible Low-Temperature Metal Node Distortion during Atomic Layer Deposition of Al_2O_3 and TiO_2 on UiO-66-NH_2 Metal-Organic Framework Crystal Surfaces. *ACS Appl. Mater. Interfaces* **2017**, *9*, 22042−22054.
(46) Feng, L.; Yuan, S.; Zhang, L.-L.; Tan, K.; Li, J.-L.; Kirchon, A.; Liu, L.-M.; Zhang, P.; Han, Y.; Chabal, Y. J.; Zhou, H.-C. Creating Hierarchical Pores by Controlled Linker Thermolysis in Multivariate Metal-Organic Frameworks. *J. Am. Chem. Soc.* **2018**, *140*, 2363−2372.
(47) Vandichel, M.; Hajek, J.; Ghysels, A.; De Vos, A.; Waroquier, M.; Van Speybroeck, V. Water Coordination and Dehydration Processes in Defective UiO-66 Type Metal Organic Frameworks. *CrystEngComm* **2016**, *18*, 7056−7069.
(48) Øien-Ødegaard, S.; Bouchevreau, B.; Hylland, K.; Wu, L.; Blom, R.; Grande, C.; Olsbye, U.; Tilset, M.; Lillerud, K. P. UiO-67-type Metal-Organic Frameworks with Enhanced Water Stability and Methane Adsorption Capacity. *Inorg. Chem.* **2016**, *55*, 1986−1991.
(49) Katz, M. J.; Brown, Z. J.; Colón, Y. J.; Siu, P. W.; Scheidt, K. A.; Snurr, R. Q.; Hupp, J. T.; Farha, O. K. A Facile Synthesis of UiO-66, UiO-67 and Their Derivatives. *Chem. Commun.* **2013**, *49*, 9449−9451.
(50) Klet, R. C.; Liu, Y.; Wang, T. C.; Hupp, J. T.; Farha, O. K. Evaluation of Brønsted acidity and proton topology in Zr- and Hf-based metal-organic frameworks using potentiometric acid-base titration. *J. Mater. Chem. A* **2016**, *4*, 1479−1485.

https://dx.doi.org/10.1021/acs.chemmater.0c03889
Chem. Mater. 2021, 33, 910−920